Solid-State Dynamic Nuclear Polarization at 263 GHz: Spectrometer Design and Experimental Results

Melanie Rosay[1*], Leo Tometich[1], Shane Pawsey[1], Reto Bader[2], Robert Schauwecker[2], Monica Blank[3], Philipp M. Borchard[3], Stephen R. Cauffman[3], Kevin L. Felch[3], Ralph T. Weber[1], Richard J. Temkin[4], Robert G. Griffin[4], and Werner E. Maas[1]

Graphical Table of Contents entry (+ one sentence)

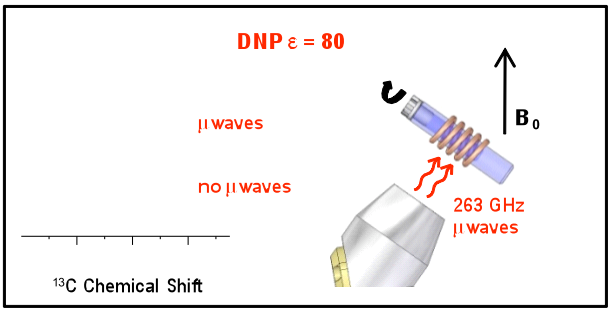

Dynamic nuclear polarization signal enhancements of up to 80 in solid samples at 95 K have been obtained using a novel 263 GHz solids DNP spectrometer with a continuous-wave gyrotron as a microwave source.

Submitted to PCCP Special Issue: High Frequency Dynamic Nuclear Polarization – The Renaissance

Author Affiliations
1. Bruker BioSpin Corporation, 15 Fortune Drive, Billerica, MA 01821, USA
*melanie.rosay@bruker-biospin.com
2. Bruker BioSpin Corporation, Industriestrasse 26, 8117 Fällanden, Switzerland
3. Communication and Power Industries, 811 Hansen Way, Palo Alto, CA 94303, USA
4. Massachusetts Institute of Technology, 77 Massachusetts Avenue, Cambridge, MA 02139, USA

Summary

Dynamic Nuclear Polarization (DNP) experiments transfer polarization from electron spins to nuclear spins with microwave irradiation of the electron spins for enhanced sensitivity in nuclear magnetic resonance (NMR) spectroscopy. Design and test of a spectrometer for magic angle spinning (MAS) DNP experiments at 263 GHz microwave frequency, 400 MHz ^{1}H frequency is described. Microwaves are generated by a novel continuous-wave gyrotron, transmitted to the NMR probe via a transmission line, and irradiated on a 3.2 mm rotor for MAS DNP experiment. DNP signal enhancements of up to 80 have been measured at 95 K on urea and proline in water/glycerol with the biradical polarizing agent TOTAPOL. We characterize the experimental parameters affecting the DNP efficiency, the magnetic field dependence, temperature dependence and polarization build-up times, microwave power dependence, sample heating effects, and spinning frequency dependence of the DNP signal enhancement. Stable system operation, including DNP performance, is also demonstrated over a 36 hour period.

1. Introduction

Solid-state NMR has been demonstrated as a powerful technique for structure determination of biological solids, in particular amyloid and membrane proteins [1-5]. However, the experiments often suffer from low sensitivity or long acquisition times due to the small polarization of nuclear spins at thermal equilibrium. DNP experiments can provide substantial enhancements in NMR sensitivity by transferring the higher Boltzmann polarization of electron spins to nuclear spins [6-9]. This polarization transfer is driven by microwave irradiation at or near the electron paramagnetic resonance (EPR) frequency. The potential gain in sensitivity can be on the order of the ratio of the electron and nuclear gyromagnetic ratios, ~ 660 for transfer from electron to ^{1}H spins and ~ 2600 for transfer to ^{13}C spins. It is difficult to reach these limits experimentally, except at very low temperature and with long polarization times such as for polarized target work and magnetic ordering [10, 11]. For solid-state NMR applications including multi-dimensional experiments significantly shorter polarization times are required. Early solid-state NMR DNP work was performed at low field of 1.4 T or less and primarily focused on materials, such as polymers or carbonaceous materials [12-16]. Applications to high field NMR were pioneered by Griffin and coauthors (MIT), using gyrotrons as a microwave source [17-22]. DNP signal enhancements of 100-300 are routinely achieved at 5-9 T (140-250 GHz EPR frequency), 90 K sample temperature, and with reasonable polarization times [23, 24]. In addition, a wide range of biological solids have been successfully polarized [25] and the mechanism of the proton pump membrane protein, bacteriorhodopsin, has been elucidated [26, 27].

A paramagnetic center, unpaired electron, is required for DNP experiments. Most of the high field DNP experiments from MIT utilize the cross effect (CE) polarization mechanism with nitroxide radicals [18] or biradicals, two nitroxide radicals tethered together for stronger electron-electron coupling [28, 29]. The CE mechanism rely on three-spin flip processes where two electrons that differ in energy by the nuclear Larmor frequency, ω_n, flip flop and the energy difference is used to flip a nuclear spin. Hence, the EPR spectrum must be wider than ω_n or two narrow lines separated by ω_n [30-32]. Nitroxide-based radicals or biradicals are well suited for DNP experiments to ^{1}H spins. In typical experiments, the sample of interest is dissolved in or mixed with a cryoprotectant solvent doped with paramagnetic centers and then frozen for DNP experiments at cryogenic temperatures. Continuous irradiation of the EPR line and ^{1}H spin diffusion facilitate distribution of the enhanced polarization throughout the solvent and solute [25, 33]. The enhanced polarization is then transferred from the abundant ^{1}H spins to a low-gamma nucleus, such as ^{13}C or ^{15}N via cross-polarization (CP) [34], prior to detection or any other solid-state NMR pulse sequence.

The CE efficiency increases with the microwave field at the sample, B_1, up to a saturation level, increases with decreasing sample temperature, and is inversely proportional to B_0 [29]. For experiments at very low temperature or with very efficient microwave delivery to a static sample, a low power microwave source may be sufficient [33, 35]. High resolution solid-state NMR experiments with magic angle spinning, MAS, have more geometrical constraints on the sample shape and surrounding components such as the MAS stator and NMR coil. The microwave irradiation of the sample may not be as efficient and higher microwave power is important. Additionally, for MAS with cold nitrogen gas (> 77 K), higher microwave power is again critical compared to DNP measurements at lower temperature. Gyrotrons can provide the necessary microwave power with stable continuous-wave (CW) operation.

Most gyrotrons are designed for military, radar, and plasma fusion applications and typically operate up to output frequency of 170 GHz with high output power, kW to MW. They are often operated with pulses of several seconds or tens of seconds, with low duty cycles; and minimal stability requirements. For DNP experiments, true continuous-wave (CW) operation for days with high frequency and power stability is required. This is especially important for structural studies where the DNP-enhanced NMR signal intensity must be stable over extended periods of time. Gyrotrons have been successfully developed and utilized by MIT for DNP applications at 140 and 250 GHz [22, 36-38] and a 460 GHz gyrotron has been experimentally demonstrated [39, 40]. More recently, a 394 GHz DNP gyrotron was designed and tested by the University of Fukui [41] and a 260 GHz gyrotron by IAP / GYCOM, N, Novgorod, Russia [42].

In this paper, we describe a DNP spectrometer with a 263 GHz gyrotron microwave source for MAS experiments at 400 MHz ^{1}H frequency, and 100 K sample temperature. The gyrotron was designed specifically for extended DNP applications with CW operation with stable frequency and output power. Details of the gyrotron design, including electron tube, magnet, and control system, are described and tuning curves are presented. The microwave beam is transmitted to the NMR probe via a corrugated transmission line and mode pattern images were taken for evaluation of the microwave beam at the sample area. DNP signal enhancements were measured on urea and proline in water/glycerol doped with TOTAPOL biradical [28, 43] at 95 K. The DNP efficiency depends on a multitude of experimental parameters including the NMR magnetic field position, sample temperature, microwave power, and spinning frequency. These effects were examined experimentally and are reported in here. Polarization build-up times and sample heating from microwave irradiation are also discussed. Finally, high stability of the gyrotron and DNP-enhanced signal intensity are demonstrated over a 36 hour period.

2. Experimental

2.1 263 GHz Gyrotron Design

Gyrotrons are cyclotron resonance masers and a special form of vacuum electronic device (VED) relying on the interaction between an electron beam and a resonant cavity condition to generate microwaves [44, 45]. All VED's share the following basic components. First, an electron gun contains a cathode and heater for electron emission, with initial electron beam acceleration when a high voltage (cathode voltage) is applied across the cathode to ground or an anode. The electron beam is further accelerated and focused through the electron tube by a magnetic field. Electron beam energy is then converted into radiation in the interaction circuit or cavity. After the cavity, the electron beam continues to the collector while the microwave beam exits the VED through the output window.

For gyrotrons, the resonance condition is achieved when the cyclotron frequency of the electrons, governed by the magnetic field, is nearly equal to the frequency of the electromagnetic cavity mode. Bunching of the electrons in the beam occurs due to the relativistic dependence of the electron mass and the electron cyclotron frequency on the electron energy. Electrons that are out of phase with the electromagnetic wave are decelerated, which causes them to lose relativistic mass and move forward in phase. Electrons that are in phase with the electromagnetic wave are accelerated and gain relativistic mass, which causes them to move backward in phase. The electrons thus form a bunch in phase space

which is rotating at nearly the frequency of the electromagnetic wave and allows for the efficient transfer of energy from the beam to the wave. The cylindrical gyrotron cavities can be overmoded. Therefore, the cavity dimensions are not limited by the wavelength and gyrotrons can produce high output power even at frequencies above 30 GHz where the performance of other types of VED's declines rapidly. More detailed information on gyrotron components and operating principles can be found in several recently published books and articles [22, 44-50]

Gyrotron Tube. A solid model and photograph of the 263 GHz gyrotron tube are shown in Figure 1. It is a hard-sealed gyrotron tube, with welded and brazed vacuum joints. After assembly, the tube is processed at high temperature for several days to reduce gas pressure and improve operability. Details of the gyrotron tube key elements, electron gun, interaction cavity, internal mode converter, output window, and collector are described below.

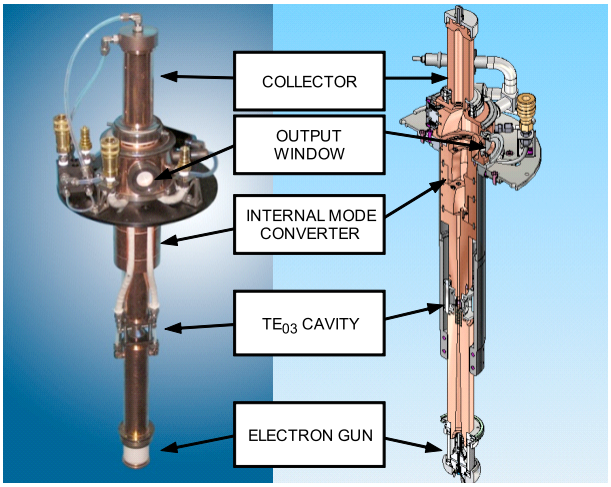

Figure 1. Photograph and solid model cross section of 263 GHz gyrotron tube.

Electron gun. A single-anode, or diode, magnetron-injection gun (MIG) was designed to operate at a nominal accelerating voltage, cathode voltage, of 11-15 kV and electron beam currents in the range of 20 – 100 mA. The average cathode radius is 0.5 cm and the average cathode loading, at 50 mA beam current, is less than 1 A/cm^2. The cathode angle and the electrode shapes were optimized to minimize the electron perpendicular velocity spread, which is predicted to be less than 1% at the nominal velocity pitch factor, α, the ratio of transverse to axial electron velocity, of 2.0. The cathode includes a filament heater for electron emission. The magnetic field is generated by a 9.7 T superconducting magnet and the ratio of

the magnetic field at the cathode to the magnetic field in the interaction cavity is 26.5. The distance from the cathode to the cavity is approximately 25 cm and the region between the electron gun and the cavity, the beam compression region, includes alternating copper and lossy-ceramic rings to prevent oscillations.

Interaction cavity. The interaction cavity was designed to support the transverse electric $TE_{0,3,1}$ mode at 263 GHz. The cavity, which consists of an input taper, a straight section, and an output taper, is predicted to have a cold quality factor, Q, of 6000 and an output mode purity of 99.7%. The calculated peak power density in the cavity, including the non-ideal effects of copper, is 47 W/cm^2 for a nominal output power of 40 W. Because the diffractive cavity Q is 6,000, nearly equal to the ohmic cavity Q, approximately half of the power generated in the cavity is lost in the cavity walls.

Multi-mode efficiency calculations were carried out with a self-consistent, time-dependent code [51]. Potential competing modes, including the $TE_{2,3,1}$, the $TE_{5,2,1}$, and $TE_{0,2,3}$ modes, were evaluated and found to have higher starting currents than the desired $TE_{0,3,1}$ mode for the nominal beam, cavity, and magnetic field parameters. Single-mode operation in the $TE_{0,3,1}$ mode was also predicted to cover a wide range of operating parameters. Large signal modeling indicated that, for a cathode voltage of 15 kV, a beam current of 30 mA, and a velocity pitch factor of 2.0, more than 100 W of power would be generated in the $TE_{0,3,1}$ mode of the cavity, resulting in more than 50 W of power at the cavity exit. Key design parameters of the interaction cavity are shown in Table 1.

The cavity was designed to be thermally isolated from the gun and internal converter regions of the gyrotron to allow for frequency tuning with varying inlet temperatures of the cavity coolant water at a rate of approximately 4 MHz/degree C.

Parameter	**Design Value**
Operating Mode	$TE_{0,3,1}$
Cold Q	6000
Frequency (GHz)	263.58
Cathode Voltage (kV)	15
Beam Current (mA)	30
Output Power	50 W
Efficiency	11%

Table 1. Design parameters for the interaction cavity.

Internal mode converter. The internal mode converter was designed to transform the annular $TE_{0,3}$ mode produced in the cavity to a Gaussian beam that exits the gyrotron through the output window perpendicular to the beam axis. The converter consists of a simple helically cut Vlasov launcher [52] and five focusing and steering mirrors, designed to direct the beam out of the region of the gyrotron in the magnet bore and to focus the Gaussian beam waist to the correct size and position to exit through the window and couple to 19.3 mm ID corrugated waveguide. Because of the non-optimized launcher, the limited space afforded by the magnet bore, and the extended axial distance traveled by the microwave beam from the cavity to the window, the calculated diffraction losses for the internal converter system were as high as 7% and the output mode purity was expected to be no greater than 90%. Cold tests (low power) were performed to align the mirrors and verify the properties of the output beam.

Output window, matching unit and gap filter. The output window consists of a single 0.093-cm thick disk of Al_20_3 with a clear aperture of 2.54 cm. Since the incident power and subsequent losses in the window disk are low, the predicted temperature rise with no direct cooling is less than 5 ºC, which offers a large margin of safety for mechanical stresses. A matching unit at the gyrotron window provides a DC electrical break and supports and centers a segment of 19.3 mm ID corrugated waveguide. This first segment is followed by a gap filter with water-cooled Teflon tubing and adjustable horizontal gap length, which absorbs unwanted stray radiation.

Collector. The collector consists of a 2-cm diameter cooled copper section designed to dissipate the spent electron beam, which follows the natural trajectories dictated by the magnetic field of the superconducting magnet. The predicted peak power loading is 250 W/cm^2 resulting in a predicted temperature on the vacuum wall of the collector of about 100 ºC.

Gyrotron magnet. A magnet is required for electron beam acceleration, beam compression to the cavity and decompression to the collector, and electron cyclotron resonance in the cavity region. The 263 GHz gyrotron magnet shown in Figure 2 is a persistent superconducting magnet with two independent magnetic centers, one in the cavity region and one in the electron gun region. The nominal field for the cavity coil is approximately 9.7 T while the gun coil can be independently adjusted for gyrotron testing

and optimization. The magnet configuration provides a good compromise between short gyrotron tube length and reasonable magnet length for a cryogenically-cooled magnet. The magnet is actively shielded with 1 meter radial 5 Gauss line. The microwave beam exits the gyrotron tube transverse to the bore axis above the magnet top plate.

Figure 2. Photograph of 263 GHz gyrotron showing from left to right: microwave transmission line, gyrotron magnet with tube installed, gyrotron control system console, and two chiller units.

Gyrotron control system. The control system monitors and controls a set of components and parameters for safe and stable operation of the 263 GHz gyrotron. It was designed on a PXI platform from National Instruments using LabWindows/CVI to develop the software, and is contained in a single-bay cabinet plus two water chillers. A wide range of operating parameters, such as the electron beam voltage and current, body current, tube vacuum, water flow and temperature, gun cooling gas flow, gyrotron magnet and waveguide connection, are continuously monitored and compared to threshold fault values. Two layers of automatic shutdown conditions are built into the system to protect from potential personal injury or instrumentation damage. Critical faults are handled directly through hardware with fast shutdown time while non-critical errors are handled through the software.

The gyrotron microwave power and frequency depend on the cathode voltage, electron beam current, cavity temperature, and magnetic field, all of which must be stable for constant output power and frequency. The high voltage power supply is a modified 4 kW Spellman x-ray power supply (DF series) with filament heater and high stability on the cathode voltage. The electron beam current is stabilized via a proportional-integrative (PI) controller which adjusts the filament current. There are two separate water circuits with PI controllers, one for the cavity with low heat load but high stability requirement, and one for the collector and tube body with higher heat load but lower stability requirements (chillers from

Optitemp). Cooling and heating elements are included in the cavity circuit to cover a temperature range of 12 to 35 ºC for frequency tuning. The control system also contains a power supply for the gyrotron tube 2 l/s VacIon pump and pressure regulator for gas cooling of the electron gun.

2.2 263 GHz transmission line and instrumentation for power and frequency measurement

The microwave beam output of the gyrotron matching unit and gap filter couples into a 19.3 mm ID corrugated transmission line. The transmission line is precision machined in 25cm long aluminum segments that are joined together by coupling clamps and held on an extruded aluminum support rail. Individual corrugations are cut with a period of 1/3 wavelength and 1/4 wavelength depth and length [53]. Three flat-mirror 90º miter bends are included in the transmission line as the microwave beam travels across the gyrotron magnet top plate, down to a horizontal support rail, across to the NMR magnet, and up to the NMR probe base. The first horizontal segment above the gyrotron magnet, vertical rail, and start of long horizontal rail can be seen in Figure 2. The distance between the two magnet bores is 2.9 meters. After the third miter bend, at the probe base, a Lucite sleeve provides a DC break and an adjustable vertical gap between the 19.3 mm transmission line and probe waveguide, followed by a corrugated taper to 7.6 mm ID. The 7.6 mm ID probe waveguide is machined from phosphor bronze and helically tapped with an M8x40 tap. The probe waveguide ends with two closely-spaced miter bends, 54.7º followed by 90º, for microwave irradiation transverse to the NMR sample rotation and coil axis. The microwave beam is launched directly to the NMR sample from the 7.6 mm ID waveguide after the 90 degree miter bend. A 7 mm diameter hole is cut through the bottom of the MAS stator and the center turns of the NMR coil are spaced out for improved microwave penetration.

A directional coupler, consisting of a 0.96 mm thick quartz plate at a 45 degree angle, is included in the transmission line for frequency and power measurements [54]. Microwave power is monitored on the forward port with frequency measurement or an absorbing load placed on the reflected port. A Scientech laser calorimeter (AC2500 and S310D display) is used for power measurement with black paint coating on the calorimeter surface to increase absorption at 263 GHz. Alternatively, a WR-3.4ZBD zero-bias detector diode from Virginia Diodes can be utilized with additional attenuation after the directional coupler. Microwave power can also be measured directly in line with a water load (calorimetric measurements) consisting of fully absorbing water-filled Teflon tubing in an aluminum housing, with temperature sensors for measuring the input and output water temperatures and a flow meter. The water load is used for calibration of the directional coupler and laser calorimeter and power measurements on

transmission line components. Frequency measurements are performed with a frequency locked tunable 24 GHz local oscillator source with better than 2 ppm frequency accuracy from Bruker BioSpin and a WR-3.4 harmonic mixer from Virginia Diodes. The resulting intermediate frequency from 11th harmonic mixing is detected on an oscilloscope after amplification and filtering.

During the intial gyrotron tests, power and frequency were measured directly at the gyrotron window using a calorimetric water load for power measurement and a spectrum analyzer (Tektronix 2784) with a 175-325 GHz harmonic mixer (Tektronix WM782J) for frequency measurement. The water load has typical error bars of ± 3% and can measure powers as low as 0.4 W. Beam images were recorded with an infrared camera (FLIR ThermaCam SC640), burn paper, and liquid crystal paper.

2.3 NMR Spectrometer and DNP measurements

DNP experiments were performed on a Bruker BioSpin Avance III 400 Wide Bore NMR spectrometer equipped with a 3.2 mm quadruple resonance H/^{13}C/^{15}N/electron low temperature magic angle spinning (LTMAS) probe and cooling cabinet. Three independent gas channels- bearing, drive, and variable temperature (VT)- are cooled through a liquid nitrogen heat exchanger enabling MAS experiments at 95-100 K and up to 14 kHz spinning frequency with ± 2 Hz stability [55]. The heat exchanger was designed specifically for low temperature MAS applications to provide sample rotation stability at the lowest temperature possible. The temperatures of all three gas channels are monitored and regulated by a BVT3000 LTMAS temperature control unit. The LTMAS probe has sample insert and eject capabilities at low temperature and samples were inserted into the pre-cooled probe, spun up and allowed to thermally equilibrate for approximately 10 minutes before any measurements were performed. The magic angle was set at low temperature using potassium bromide, KBr, and shimming on KBr and N-acetyl-valine and KBr. Typical NMR acquisition parameters are 100 kHz field on ^{1}H channel with TPPM [56] or SPINAL 64[57] decoupling, 55-60 kHz on ^{13}C CP, 40-45 kHz on ^{15}N CP, 10% ramp on ^{1}H during CP, 0.5-3 ms CP contact time, 20-50 ms acquisition time, 2-10 seconds recycle delay depending on relaxation time and signal intensity.

The LTMAS probe includes the 263 GHz probe waveguide detailed in Section 2.2. All reported DNP measurements were performed using gyrotron tube serial number one which operates at 15 kV cathode voltage, 60 mA beam current, 27.5 ºC cavity temperature, and 263.343 GHz microwave frequency. The NMR field is set to 399.90 MHz ^{1}H frequency. DNP experiments were performed with the gyrotron on continuously and with cross polarization from ^{1}H to ^{13}C or ^{15}N. Therefore, the reported

DNP signal enhancements are from the enhanced ^{1}H spins. The DNP signal enhancement is calculated by comparison of the NMR signal intensities or integrals with and without microwave irradiation. The microwave power at the end of the probe waveguide was 5.5-6 W unless otherwise specified. Error bars, typically 1-2%, in the DNP signal enhancement measurements arise from the higher noise level of the spectrum without microwave irradiation. Spin lattice relaxation times, T_1, and DNP build-up times, τ, were recorded with saturation recovery pulse sequences and analyzed with the T1/T2 relaxation module in TopSpin.

2.4 Sample preparation and EPR measurements

All DNP samples were prepared with TOTAPOL biradicalSong, 2006 #31} in glycerol-d8/D_20/H_20 solution with 60/30/10 volume ratio, unless otherwise specified. Liquid samples were transferred by pipette into 3.2 mm OD, 2.2 mm ID sapphire or zirconia rotors with 30 µl active sample volume. Only 22-25 µl sample volume was actually utilized to leave sufficient space for soft Silicone sealing plugs that are inserted above the liquid sample to prevent any sample leakage before the sample was frozen. Zirconia drive caps are used for low temperature experiments. Unused filled rotors are stored in the freezer with the sealing plug still in place.

The actual nitroxide radical concentration was measured by EPR spectroscopy at 9.8 GHz using a Bruker BioSpin EMX-Plus spectrometer. Packed and sealed 3.2 mm rotors fit in a 4 mm ID EPR tube. The nitroxide concentration was calculated using the Xenon software. The spin count measures the nitroxide spin concentration independent of its form, mono radical or biradical. The TOTAPOL concentration was calculated by dividing the nitroxide concentration from the spin count by two, assuming that all the measured nitroxide spins are in biradical form. EPR measurements indicated 20-50% lower TOTAPOL concentration than expected from calculated concentrations indicating errors in the sample preparation or impurities in the TOTAPOL.

2.5 Temperature calibration

The spin lattice relaxation time, T_1, of ^{79}Br in KBr was used as a thermometer following the methods detailed in Thurber et al. for temperature calibration[58]. KBr was tightly packed into 3.2 mm zirconia and sapphire rotors and sealed with PTFE spacers. The spin-lattice relaxation times were recorded with a saturation recovery pulse sequence comprising 11 data points corresponding to delays from 10 ms to 15 s. Spectra for the zirconia rotor sample were collected at MAS spinning frequencies of 12.5, 8.5 kHz and

static conditions, from 100 K to 205 K. For the sapphire rotor, T_1 was recorded from 6 KHz to 14 kHz MAS frequency in increments of 2 kHz and for a static sample, all at 100 K. The actual sample temperature was calculated from the T_1 value of the ^{79}Br nuclei in KBr using previously described methods [58] and used for calibration of two thermocouples in the probe, the stator exhaust temperature and the thermocouple in the variable temperature line. The calculated sample temperature was lower than the thermocouple readings for both rotors. The sample temperatures reported in this paper correspond to the calibrated values with no microwave irradiation on.

The KBr T1's were measured with the gyrotron on and off for the zirconia and sapphire rotor to measure the sample heating due to microwave irradiation. Additionally, to measure temperature rise in an actual frozen DNP sample a quartz capillary, 0.5 mm ID, 0.7 mm OD, approximately 5 mm in length was packed with KBr and sealed with an epoxy resin. The capillary was mounted into a PTFE spacer so that only the epoxy seal was in the spacer. The capillary and spacer were then placed into a 3.2 mm sapphire rotor filled with glycerol-d8/D_20/H_20 60/30/10 volume ratio stock solution with 10 mM TOTAPOL and closed with a zirconia drive cap. This was done in a manner so that the KBr in the capillary was surrounded by the DNP stock solution. The T_1 values of the capillary samples were recorded under static and 1.2 kHz spinning frequency also at 100 K.

3. Results and Discussion

3.1 263 GHz gyrotron test

Four nominally identical gyrotron tubes were fabricated and demonstrated. A summary of the typical test sequence and measured data for gyrotron tube serial number 4 follows.

During the initial tests, beam voltage, beam current, magnetic field in the cavity region, and magnetic field in the electron gun region were systematically varied to determine the parametric limits and to select a nominal operating point. Figure 3a shows the measured output power and efficiency as a function of beam current for a cathode voltage of 12 kV and a fixed magnetic field. Output powers of 20 to 90 W and efficiencies up to 10% were measured for beam currents from 25 to 75 mA. To obtain lower output power, the cathode voltage can also be adjusted as shown in Figure 3b, where the output power varies smoothly from 90 W to less than 2 W by varying cathode voltage from 12.8 kV to 10 kV while holding the magnetic field and filament power fixed and allowing the beam current to fall naturally as the

voltage is reduced. For the measurement, the cavity coolant temperature was held constant at 20 ºC and the frequency varied from 263.59 GHz to 263.52 GHz as the power was tuned.

To achieve smooth power tuning with cathode voltage while maintaining a constant frequency, the inlet temperature of the cavity cooling water can be varied. Figure 3c shows the measured change in output frequency as a function of cavity coolant temperature with the beam voltage and beam current held fixed at 12 kV and 50 mA, respectively, and all other parameters kept constant. As shown in the figure, the output power does not vary as a function of cavity coolant temperature and the frequency varies with the coolant temperature at a rate of 4 MHz/ºC from 10 to 38 ºC. The ability to tune the frequency by varying the cavity coolant temperature was exploited to maintain a constant frequency while output power is varied, as shown in Figure 3d.

During the initial experimental demonstration, the gyrotron was routinely operated continuously for days without fault. Also, it was demonstrated that the gyrotron could operate without fault with 100% of the power reflected back into the device through the output window. Slightly elevated gas levels indicated some additional heating in the gyrotron tube due to the reflected power, but the gyrotron operated without fault at parameters that would have yielded 40 W output power with no reflection present.

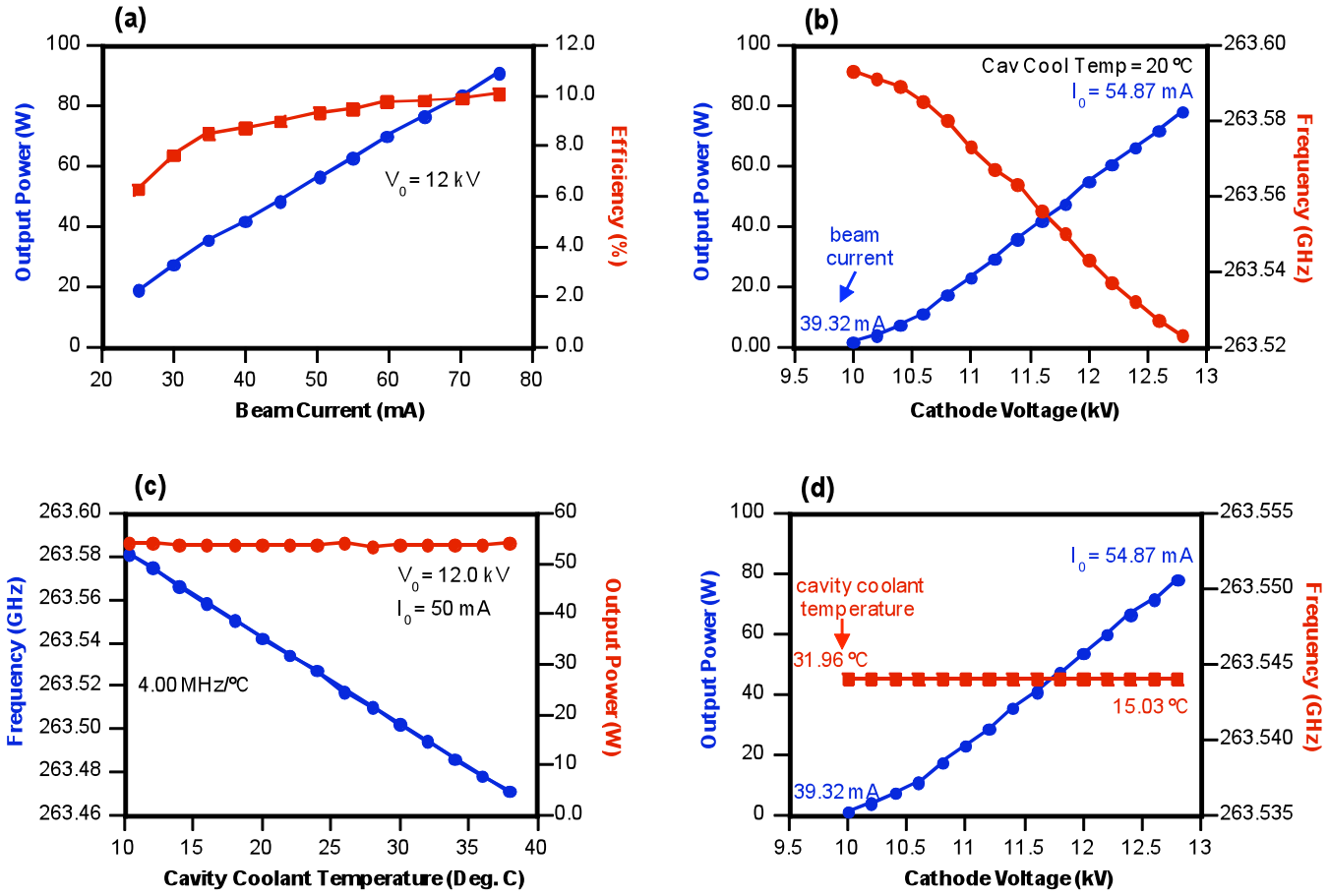

Figure 3. 263 GHz gyrotron tuning curves: **(a)** Output power (blue circles) and efficiency (red squares) as function of electron beam current at 12 kV cathode voltage, V_0. **(b)** Output power (blue circles) and frequency (red circles) versus beam voltage for fixed cavity inlet coolant temperature (20 ºC), magnetic field, and filament power. The beam current, I_0, varied, as indicated on the plot. **(c)** Frequency (blue circles) and output power (red circles) as a function of inlet cavity coolant temperature with all other parameters fixed. **(d)** Output power (blue circles) and frequency (red squares) versus beam voltage for fixed magnetic field and filament power. The cavity inlet coolant temperature is adjusted to maintain a constant frequency, 263.544 GHz.

3.2 Mode pattern measurements at the sample

The gyrotron output microwave beam is transmitted to the sample through a metallic corrugated waveguide transmission line. The microwaves are launched from the end of the probe waveguide and form a Gaussian-like beam in free space directed at the sample. Infrared images of the microwave beam were obtained to verify the beam pattern at the DNP sample area. A paper target was positioned perpendicular to the waveguide exit and IR images in planes at varying distances of 2.5 cm to 20.3 cm from the waveguide were made. Figure 4 shows the images at 2.54 cm (1 inch) and 10.16 cm (4 inches) from the probe waveguide exit. As is evident in the figure, the microwave power exits the waveguide as a

high quality Gaussian beam that is centered and directed at the sample. The distance from the end of the waveguide to the center of the sample is 13.4 mm and the beam waist (radius at which the amplitude is 1/e of the peak value) is estimated at 3.4 mm based on images closest to the waveguide and the expansion out. This beam waist matches well to the NMR sample size, a cylinder with 2.2 mm diameter (rotor ID) and 5 mm length.

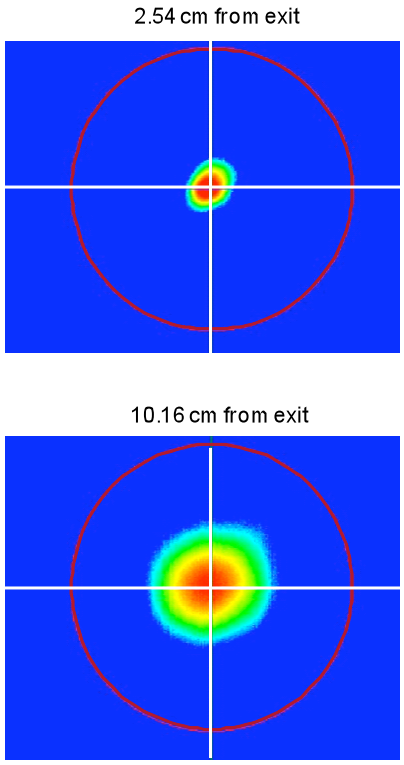

Figure 4. Infrared images of microwave beam exiting the 7.6-mm diameter probe waveguide after the final miter bend. The target was positioned perpendicular to the waveguide exit. The cross hairs indicate the center of the waveguide and the red circles denote a 7.6 cm diameter.

3.3 DNP measurements on standard samples and characterization of experimental parameters

DNP signal enhancement of urea and proline standard samples. Initial DNP experiments were performed on a ^{13}C-urea and uniformly labeled ^{13}C, ^{15}N-proline samples dissolved in glycerol/water with 15 mM TOTAPOL. A typical DNP pulse sequence for a CPMAS experiment is shown in Figure 5a. The microwaves are on continuously and any solid-state NMR pulse sequence can be performed. DNP signal enhancements of up to a factor of 80 were measured on urea at spinning frequency, $\omega_r/2\pi$, of 5

kHz, and up to 70 on proline at $\omega_r/2\pi$ = 8 kHz MAS, both at 95 K sample temperature. The ^{13}C CPMAS spectra of the proline sample with and without DNP are shown in Figure 5b and excellent sensitivity can be seen in the DNP-enhanced spectrum with just 8 second of data acquisition. These results are consistent with previously published DNP signal enhancement factor of 100-115 at 250 GHz and slightly lower temperature [59, 60].

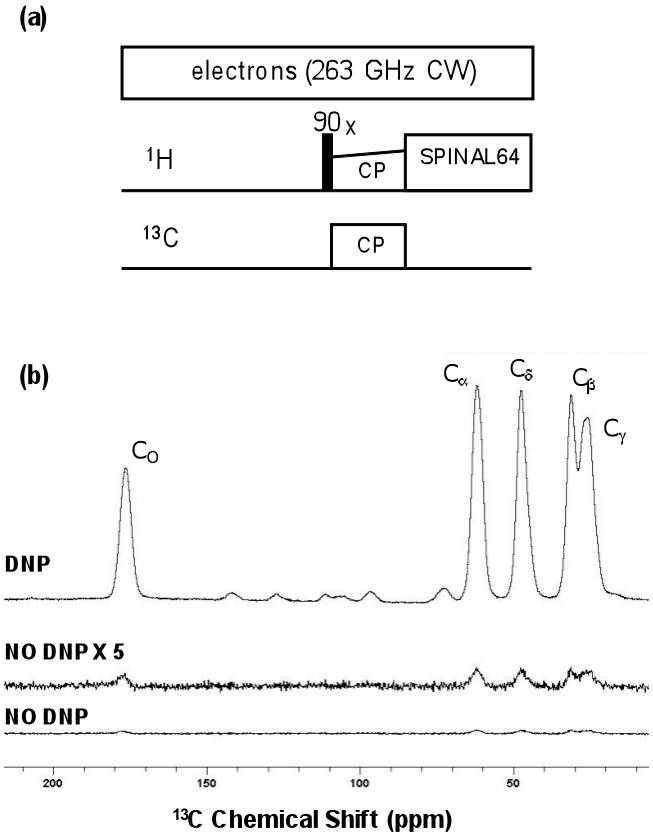

Figure 5. (a) DNP CPMAS pulse sequence, (b) Spectra of 0.5 M U- ^{13}C, ^{15}N-Proline in glycerol-d8/$d_2$0/$H_2$0 (60/30/10 volume ratio) and 15 mM TOTAPOL biradical, 25 µl sample volume, with DNP (top trace) and without DNP (bottom traces). Spectra acquired at $\omega_r/2\pi$ = 8 kHz MAS, 95 K sample temperature, with 8 scans, 2 s recycle delay, and one dummy scan. Higher numbers of scans were also acquired with microwaves off for more accurate DNP signal enhancement calculation.

Field dependence curve. The DNP signal enhancement varies as a function of irradiation position within the EPR line. Since the gyrotron frequency has a limited tuning range compared to the width of the TOTAPOL EPR line, the NMR magnetic field was swept while the gyrotron frequency remained constant. The resulting field dependence curve plotting DNP signal enhancement as a function of NMR ^1H frequency is shown in Figure 6. The curve has a base-to-base width of 410 Gauss (1.15 GHz) and follows the expected profile for nitroxide biradicals via the cross effect DNP for ^1H spins [29]. The gyrotron frequency tuning range of 100 MHz (35 Gauss) with the cavity temperature allows for local

tuning about the maximum position of the field dependence curve. Following the field sweep, the NMR field position was set to the positive maximum of the curve.

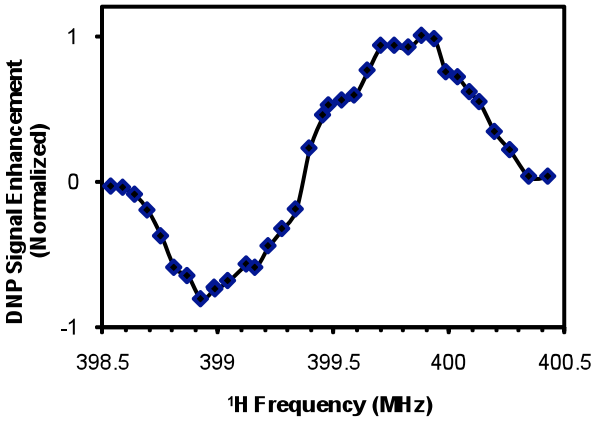

Figure 6. Field dependence curve on 2 M ^{13}C Urea in glycerol-d8/D_20/H_20 (60/30/10 volume ratio) with 15 mM TOTAPOL biradical. The NMR field was swept while the gyrotron remained at fixed frequency, 263.343 GHz. Each field position was measured with ^{13}C CPMAS experiment with microwaves on and off for calculating the DNP signal enhancement. 4 scans, 10 s recycle delay, and 2 dummy scans per experiment, $\omega_r/2\pi$ = 5.1 kHz, 105 K sample temperature. Error bars on the DNP signal enhancement measurements are ± 2%.

Temperature dependence and polarization build-up times. The cross effect polarization transfer is more favorable at low temperature due to longer electron and proton relaxation times [59] and the first high field DNP experiments using nitroxide radicals were performed at ~ 20 K at 140 GHz static and with MAS at 60 K [18, 19]. The helium temperature experiments were followed by nitrogen temperature experiments at 140 and 250 GHz [20, 21, 26]. Figure 7 shows the temperature dependence of the ^{1}H DNP signal enhancement from 97 K to 160 K at 263 GHz with TOTAPOL biradical as polarizing agent. The DNP efficiency increases steeply as the temperature approaches 95 K and larger DNP signal enhancements should be observed at lower temperatures using helium-temperature probes [19, 61, 62]. Reasonable DNP efficiency can still be observed at higher temperature, with a factor of 10 signal enhancement measured at 150 K on the urea sample, expanding high-field CE DNP experiments to a higher temperature range than previously reported. Additionally, it is clear that the sample temperature must be stable for constant DNP signal enhancement during long experiments.

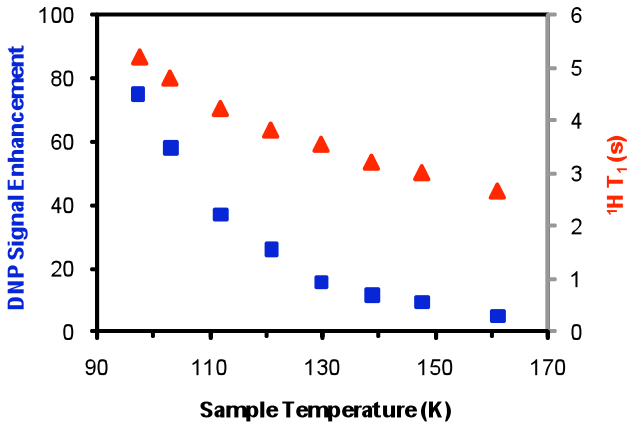

Figure 7. Temperature dependence of the ^{1}H DNP signal enhancement (blue squares) and ^{1}H spin lattice relaxation times, T_1, (red triangles) measured on 2 M ^{13}C Urea in glycerol-d8/D_20/H_20 (60/30/10 volume ratio) with 15 mM TOTAPOL biradical. Each temperature point was measured with microwaves on and off for the DNP signal enhancement calculation. ^{13}C CPMAS experiments with 4 scans, 10 s recycle delay, 2 dummy scans, $\omega_r/2\pi$ = 6.2 kHz, with microwaves on and off for calculation of the DNP signal enhancement. ^{1}H T_1 was measured with ^{1}H saturation recovery with CP detection, 11 points and 2 scans per point. Standard deviation was less 1 x 10^{-2} on the calculated T_1 values. Error bars on the DNP signal enhancements are ± 2%. Sample temperature corresponds to calibrated temperature with the microwaves off.

The ^{1}H spin lattice relaxation times, T_1, were also measured as a function temperature using a saturation recovery CPMAS experiment and are plotted in Figure 7. For both the urea and proline samples, the ^{1}H T_1's measured in the glycerol solvent and the urea or proline solute are identical and also similar to the polarization build-up time (saturation recovery experiment with the microwaves on). The time constants can differ between solvent and solute in the case of macroscopic samples, for example in amyloidal nanocrystals [25]. For NMR experiments requiring signal averaging with multiple scans, both the DNP signal enhancement and the polarization time must be considered as excessive polarization times can offset the gains from DNP signal enhancement. In the temperature range of 97-160 K, net gains in sensitivity-per-unit-time are still obtained by going to lower temperature. Higher radical concentration can also be used to shorten T_1. In bacteriorhodopsin this works well because the TOTAPOL is excluded from the bilayer membrane [60]

Deuterated solvents have been used to further enhance sensitivity for ^{1}H DNP experiments followed by CP to low abundance nuclei [28, 29, 63]. Figure 6 shows the polarization build-up for 0.1 M proline in two different stock solutions, glycerol-d8/D_20/H_20 (60/30/10 volume ratio) and fully protonated glycerol/H_20 (60/40 volume ratio), both with 10 mM TOTAPOL. The 90% deuterated solvent has a DNP signal enhancement of 63 while the protonated sample measures a factor of 42. The polarization build-up

time constant is a slightly longer with deuterated solvent, 4.56 seconds versus 4.14 seconds. Still, a net gain in sensitivity is obtained with solvent deuteration. The CP match condition can become much sharper with highly deuterated solvents, so a balance must be achieved between the DNP and CP efficiency.

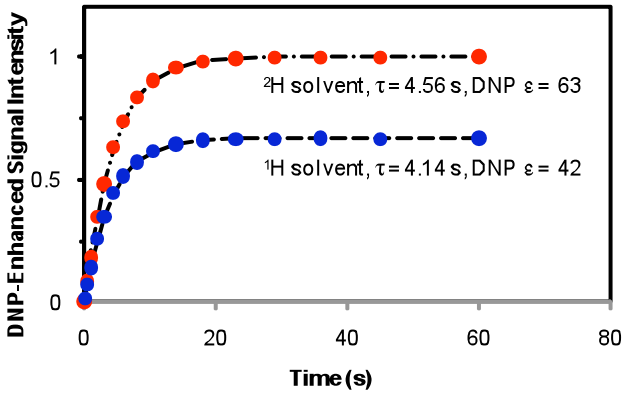

Figure 8. DNP polarization build-up and signal enhancement for 0.1 M U-^{13}C-^{15}N-Proline in glycerol-d_8/$D_2$0/$H_2$0 (60/30/10 volume ratio), red circles, and in glycerol/$H_2$0 (60/40 volume ratios), blue circles, both with 10 mM TOTAPOL. Polarization build-up measured with ^{1}H saturation recovery with ^{13}C CP detection and normalized to maximum value, 4 scans per point, $\omega_r/2\pi$ = 8 kHz, 97 K sample temperature, microwaves on continuously. The dotted lines are the fit with the calculated T_1 values from the TopSpin T_1/T_2 relaxation module.

Power dependence, sample heating, and magic angle spinning. The DNP signal enhancement as a function of microwave power at the end of the probe waveguide is shown in Figure 9. The DNP signal enhancement increases with microwave power up to a saturation level. This saturation level does not correspond to an intrinsic maximum DNP efficiency, but rather a contribution from a range of experimental parameters, such as the rotor material, beam pattern, coil design, sample temperature, etc. For example, during initial testing of different NMR coils for optimization of microwave penetration, the power curves showed the same pattern but reached a plateau at a lower maximum DNP signal enhancement. Similarly, different rotor materials lower the maximum DNP signal enhancement achieved. For zirconia rotors, the maximum DNP signal enhancement was 18-20% lower than for sapphire rotors filled with the same DNP stock solution and sample volume.

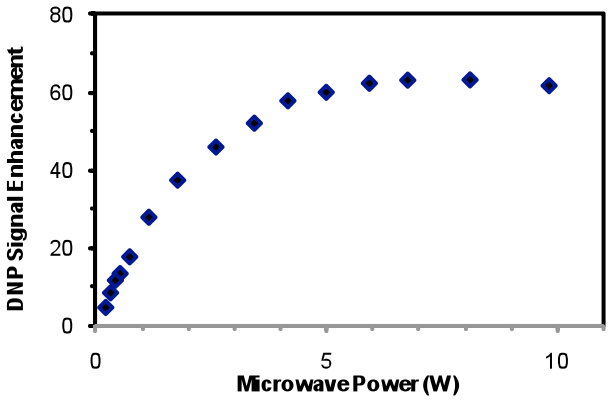

Figure 9. ^{1}H DNP signal enhancement as a function of microwave power at the end of the probe waveguide measured on 0.1 M U-^{13}C-^{15}N-Proline in glycerol-d8/$D_2$0/$H_2$0 (60/30/10) volume ratio. ^{13}C CPMAS experiment with 8 scans, 10 s recycle delay, 1 dummy scans, $\omega_r/2\pi$ = 8 kHz, 97 K sample temperature, microwaves on continuously. 64 scans were acquired for the microwave off measurement and the error bar on the DNP signal enhancement is ± 1%. The gyrotron electron beam current, cathode voltage, and cavity temperature were varied to cover the full power range with constant frequency. The microwave power was measured with the transmission line directional coupler and calorimeter, calibrated with the water load at the end of the probe waveguide.

The sample temperature rise due to microwave irradiation was measured using a sealed KBr quartz capillary (0.7 mm OD) in a sapphire rotor (2.2 mm ID) filled with glycerol-d_8/$D_2$0/$H_2$0 and 10 mM TOTAPOL. The temperature of the capillary sample was calculated from KBr T1 measurements [58]. For a static sample, the sample temperature increased by more than 15 K upon microwave irradiation. At $\omega_r/2\pi$ = 1.2 kHz, the sample temperature increased by 8-9 K. The temperature rise due to microwave irradiation was also measured in sapphire and zirconia rotors fully packed with just KBr. For the sapphire rotor packed with KBr powder, a 4 K temperature rise with microwave irradiation was measured for static experiments, 1-2 K for $\omega_r/2\pi$ = 1.5 kHz, and < 1 K for $\omega_r/2\pi$ = 8 kHz. The zirconia rotor filled with KBr experienced 11-12 K sample heating in static experiment and 4 K heating at $\omega_r/2\pi$ = 12.5 kHz. All measurements were performed with 6 W of microwave power at the end of the probe waveguide.

Sample spinning reduces microwave heating since the microwave irradiation is transverse to the sample rotation axis and different parts of the sample are heated during a rotation period. It is also beneficial for more uniform microwave irradiation of the sample. Additionally, for DNP experiments using a polarizing agent with an EPR line broadened by g-anisotropy in a static configuration only a subset of electron spins are on-resonance with microwave irradiation and take part in the DNP process. During MAS, more electron spins are cycled through a resonance condition with the microwave frequency [64]. These factors contribute to the observed dependence of the DNP signal enhancement on the

MAS frequency, shown in Figure 10. The DNP signal enhancement increases quickly from static experiment to $\omega_r/2\pi$ = 3 kHz, reaches a maximum efficiency around 3 kHz, and then decreases as the spinning frequency is further increased. We have observed from the KBr temperature measurements that for constant bearing, drive, and VT gas temperatures entering the MAS stator, the actual sample temperature in the sapphire rotor increases by 4 K from static to 8 kHz MAS spinning frequency and an additional 5 K from 8 to 12 KHz. Recalling the temperature dependence in Figure 7 it is clear that increased sample temperature due to MAS would have an adverse effect on the DNP efficiency and comparison of the two data sets indicates that the decrease in DNP efficiency from 8 to 12 kHz spinning frequency is in qualitative agreement with the expected sample temperature rise due to sample spinning. For example, there is a 22% drop in DNP efficiency from $\omega_r/2\pi$ = 8 to 12 kHz and 23% drop in DNP efficiency from 97.3 K to 103.0 K.

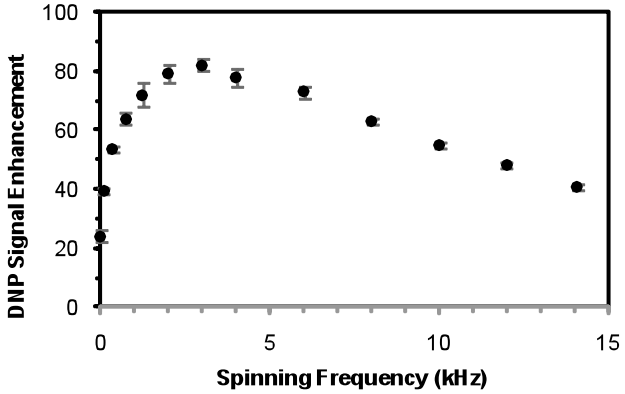

Figure 10. Spinning frequency dependence of the ^{1}H DNP signal enhancement of 0.1 M U-^{13}C-^{15}N-Proline in glycerol-d8/D_20/H_20 (60/30/10 volume ratio), measured with ^{13}C CPMAS experiment at 97 K. Spectra were measured with and without microwave irradiation at each spinning frequency for calculation of the DNP signal enhancement. 10 s recycle delay, 1 dummy scans, 16 to 64 scans per experiment depending on the spinning frequency. Error bars are indicated on the plot.

3.4 System stability for extended experiments

NMR measurements with hours or days of signal averaging time require stable experimental conditions. Gyrotron parameters that provided the frequency and power tuning capabilities described in Section 3.1 must now be held constant. Stable gyrotron and DNP operation was demonstrated during a 36 hour run. The NMR signal intensity of the $^{13}C_{\delta}$ resonance of proline in water/glycerol with TOTAPOL is shown in Figure 11 recorded as a series of ^{13}C CPMAS experiments. The spinning frequency was regulated by the MAS controller at 8 kHz ± 2 Hz and the temperature by the BVT3000 LTMAS to within ± 0.1 degree of

set value on all three gas channels. The DNP-enhanced signal intensity variation is less than ± 1% for the largest observed deviations (0.31% standard deviation). The 36 hour gyrotron on period was followed by 80 minutes with the gyrotron off and a 2 hour back on period before final off, with the NMR acquisition continuing during all time periods. During the gyrotron off segment, the cathode voltage is set to zero while the filament current remains at its last value before the gyrotron was turned off. When the gyrotron is turned back on, the cathode voltage increases gradually to 15 kV over approximately 30 seconds. The electron beam current briefly overshoots the target value and is then within 4 minutes regulated back down. The NMR signal intensity also takes a few minutes to stabilize, due to the cathode voltage ramp, electron beam current overshoot, and the equilibration time for the increase in sample temperature from microwave irradiation. Nevertheless, 5 minutes from when the gyrotron was turned back on, the NMR signal intensity had returned to within ± 1% of its average value during the 36 hour run. Detailed information including stability plots on the gyrotron parameters, cathode voltage, electron beam current, microwave power measurements, gyrotron cavity temperature, and tube vacuum, can be found in Supplementary Information.

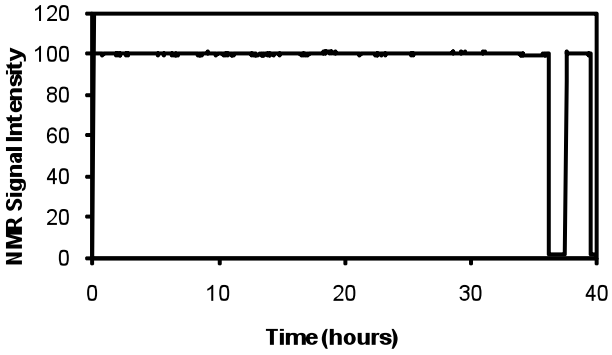

Figure 11. NMR signal intensity for $^{13}C_{\delta}$ resonance of 0.1 M ^{13}C-^{15}N Proline in glycerol-d8/D_20/H_20 (60/30/10 volume ratio) with 10 mM TOTAPOL during extended experiment run consisting of 36 hours gyrotron on, followed by 80 minutes gyrotron off, 2 hours gyrotron back on and off again. ^{13}C CPMAS experiment with 1.5 ms 55 kHz CP, 33 ms acquisition time with 100 kHz SPINAL64 decoupling, $\omega_r/2\pi$ = 1.2 kHz, 97 K sample temperature, 16 scans, 1 dummy scans, 6 second recycle delay for each point.

4. Conclusion

A 263 GHz DNP spectrometer has been designed, built, and utilized for MAS NMR experiments at ~ 100 K with enhanced sensitivity. The measured dependence of DNP signal enhancement on sample temperature, microwave power, and sample spinning frequency provide insight into the possible

parameter space for DNP experiments and highlight stability requirements for stable DNP signal enhancements. The spectrometer has been shown to have the high stability that is required for multi-dimensional experiments including correlation spectroscopy, and distance and torsion angle measurements. Examples of applications on amyloid fibrils and nanocrystals can be found in the publications by Debelouchina et al [65] also submitted to this special issue of Physical Chemistry Chemical Physics on high frequency DNP. The water/glycerol doped with TOTAPOL nitroxide biradical solvent used in the experiments is compatible with a wide range of biological solids. The enhanced sensitivity from DNP experiments and demonstrated stability should expand possible applications of solid-state NMR to samples that are otherwise unattainable due to small sample amount or dilute concentration, such as large membrane proteins or integral biological systems.

Acknowledgements

We thank Eckhard Bez, Patrick Saul, Albert Donkoh, Dr. Wurong Zhang, Dr. Michael Fey, Dr. Jochem Struppe, Dr. Frank Engelke, and Patrick Krencker of Bruker BioSpin for many valuable discussions and technical assistance. RGG acknowledges support from NIH grants EB-002804 and EB-002026 and RJT from grants EB-001965 and EB-004866 .

Supplementary Information

Stable gyrotron operation is illustrated in Supplementary Figure 1. The plots show the logged values recorded by the control system software once per second. The cathode voltage, in panel (a) was set at 15 kV and is stable to within ± 24 V (5.8 V standard deviation). The electron beam current panel (b) is stabilized with a PI controller which compares the measured value to the set point and adjusts the filament heater as needed. The electron beam current in panel (b) is stable to within ± 0.5 mA (0.09 mA standard deviation on 60.52 mA average). With constant cathode voltage and stabilized electron beam current, the output power is constant as shown in panel (c). The noise level is due to fluctuations in the calorimeter reading and is also observed when the gyrotron is off. Power measurements using the detector diode produced similar noise level. The PI controller utilizes the electron beam current as input rather than microwave power since the output power is proportional to the electron beam current with all other parameters fixed (Figure 3a) and it offers fast response time and lower measurement noise.

The cavity coolant temperature also has a PI controller for constant output frequency and is stable to within ± 0.1 ºC of the 27.5 ºC set point, panel (d). The gyrotron frequency, which was not measured during this experiment, has always been stable to within the measurement resolution of 1 MHz in previous frequency measurements. Therefore, after approximately 3 months of operation the frequency measurement assembly was removed from the directional coupler and replaced with an absorbing load. The VacIon pump pressure remained at extremely low pressure of 6 x 10^{-10} Torr during the entire run. We have seen absolutely no signs of any limitation on duration of gyrotron operation, including experimental DNP runs of up to 12 days.

XX INSERT FIGURE 11

Figure 11. Gyrotron parameter values extended experiment run consisting of 36 hours gyrotron on, followed by 80 minutes gyrotron off, 2 hours gyrotron back on and off again: (a) cathode voltage, (b) electron beam current, (c) power measurement from laser calorimeter reading calibrated with water load, (d) cavity coolant temperature, and (e) tube vacuum.

References

1. R. G. Griffin, *Nat. Struct. Biol.*, 1998, **5**, 508-512.
2. J. M. Griffiths, K. V. Lakshmi, A. E. Bennett, J. Raap, C. M. Vanderwielen, J. Lugtenburg, J. Herzfeld and R. G. Griffin, *J. Am. Chem. Soc.*, 1994, **116**, 10178-10181.
3. P. T. Lansbury, P. R. Costa, J. M. Griffiths, E. J. Simon, M. Auger, K. J. Halverson, D. A. Kocisko, Z. S. Hendsch, T. T. Ashburn, R. G. S. Spencer, B. Tidor and R. G. Griffin, 1995, **2**, 990-997.
4. C. P. Jaroniec, C. E. MacPhee, V. S. Bajaj, M. T. McMahon, C. M. Dobson and R. G. Griffin, *Proc. Nat'l. Acad. Sci.*, 2004, **101**, 711-716.
5. A. E. McDermott, *Current Opinion in Structural Bioogy*, 2004, **14**, 554-561.
6. A. Abragam and M. Goldman, *Nuclear Magnetism: Order and Disorder*, Clarendon Press, Oxford, 1982.
7. T. P. Carver and C. P. Slichter, *Phys. Rev.*, 1956, **102**, 975-980.
8. T. R. Carver and C. P. Slichter, *Physical Review*, 1953, **92**, 212-213.
9. A. W. Overhauser, *Phys. Rev.*, 1953, **92**, 411-415.
10. W. d. Boer, *Journal of Low Temperature Physics*, 1976, **22**, 185-212.
11. D. Crabb and W. Meyer, *Annu. Rev. Nucl. Part. Sci.* , 1997, **47**, 76-109.
12. M. Afeworki, R. A. Mckay and J. Schaefer, *Macromolecules*, 1992, **25**, 4084-4091.
13. M. Afeworki and J. Schaefer, *Macromolecules*, 1992, **25**, 4092-4096.
14. M. Afeworki, S. Vega and J. Schaefer, *Macromolecules*, 1992, **25**, 4100-4106.
15. D. J. Singel, H. Seidel, R. D. Kendrick and C. S. Yannoni, *J Magn Reson*, 1989, **81**, 145-161.
16. R. A. Wind, M. J. Duijvestijn, C. Vanderlugt, A. Manenschijn and J. Vriend, *Progress in Nuclear Magnetic Resonance Spectroscopy*, 1985, **17**, 33-67.

17. L. R. Becerra, G. J. Gerfen, R. J. Temkin, D. J. Singel and R. G. Griffin, *Physical Review Letters*, 1993, **71**, 3561-3564.
18. G. J. Gerfen, L. R. Becerra, D. A. Hall, R. G. Griffin, R. J. Temkin and D. J. Singel, *Journal of Chemical Physics*, 1995, **102**, 9494-9497.
19. D. A. Hall, D. C. Maus, G. J. Gerfen, S. J. Inati, L. R. Becerra, F. W. Dahlquist and R. G. Griffin, *Science*, 1997, **276**, 930-932.
20. M. Rosay, V. Weis, K. E. Kreischer, R. J. Temkin and R. G. Griffin, *J. Am. Chem. Soc.*, 2002, **124**, 3214-3215.
21. V. S. Bajaj, C. T. Farrar, M. K. Hornstein, I. Mastovsky, J. Vieregg, J. Bryant, B. Elena, K. E. Kreischer, R. J. Temkin and R. G. Griffin, *J. Mag. Res.*, 2003, **160**, 85-90.
22. V. S. Bajaj, M. K. Hornstein, K. E. Kreischer, J. R. Sirigiri, P. P. Woskov, M. L. Mak-Jurkauskas, J. Herzfeld, R. J. Temkin and R. G. Griffin, *J Magn Reson*, 2007, **189**, 251-279.
23. A. B. Barnes, G. D. Paëpe, P. C. A. v. d. Wel, K.-N. Hu, C.-G. Joo, V. S. Bajaj, M. L. Mak-Jurkauskas, J. R. Sirigiri, J. Herzfeld, R. J. Temkin and R. G. Griffin, *Applied Magnetic Resonance*, 2008, (in press).
24. T. Maly, G. T. Debelouchina, V. S. Bajaj, K.-N. Hu, C.-G. Joo, M. L. Mak-Jurkauskas, J. R. Sirigiri, P. C. A. v. d. Wel, J. Herzfeld, R. J. Temkin and R. G. Griffin, *J. Chem Physics*, 2008, **128**, 052211.
25. P. C. A. van der Wel, K. N. Hu, J. Lewandowski and R. G. Griffin, *J. Am. Chem. Soc.*, 2006, **128**, 10840-10846.
26. M. L. Mak-Jurkauskas, V. S. Bajaj, M. K. Hornstein, M. Belenky, R. G. Griffin and J. Herzfeld, *Proc. Nat'l. Acad. Sci.*, 2008, **105**, 883-888.
27. V. S. Bajaj, M. L. Mak-Jurkauskas, M. Belenky, J. Herzfeld and R. G. Griffin, *Proc. Nat'l. Acad. Sci.*, 2009, **106**, 9244-9249.
28. K. N. Hu, H. H. Yu, T. M. Swager and R. G. Griffin, *J. Am. Chem. Soc.*, 2004, **126**, 10844-10845.
29. K.-N. Hu, C. Song, H.-h. Yu, T. M. Swager and R. G. Griffin, *J. Chem. Phys.*, 2008, **128**, 052321.
30. C. F. Hwang and D. A. Hill, *Phys. Rev. Letters*, 1967, **19**, 1011-1013.
31. C. F. Hwang and D. A. Hill, *Phys. Rev. Letters*, 1967, **18**, 110-112.
32. D. S. Wollan, *Phys. Rev. B*, 1976, **13**, 3671-3685.
33. M. Rosay, A. C. Zeri, N. S. Astrof, S. J. Opella, J. Herzfeld and R. G. Griffin, *J. Am. Chem. Soc.*, 2001, **123**, 1010-1011.
34. A. Pines, M. G. Gibby and J. S. Waugh, *J. Chem. Phys.*, 1973, **59**, 569-590.
35. V. Weis, M. Bennati, M. Rosay, J. A. Bryant and R. G. Griffin, *J Magn Reson*, 1999, **140**, 293-299.
36. L. R. Becerra, G. J. Gerfen, B. F. Bellew, J. A. Bryant, D. A. Hall, S. J. Inati, R. T. Weber, S. Un, T. F. Prisner, A. E. McDermott, K. W. Fishbein, K. E. Kreischer, R. J. Temkin, D. J. Singel and R. G. Griffin, *J. Magn. Reson. Ser. A*, 1995, **117**, 28-40.
37. S. T. Han, R. G. Griffin, K. N. Hu, C. G. Joo, C. D. Joye, J. R. Sirigiri, R. J. Temkin, A. C. Torrezan and P. P. Woskov, *Ieee T Plasma Sci*, 2007, **35**, 559-564.
38. C. D. Joye, R. G. Griffin, M. K. Hornstein, K. N. Hu, K. E. Kreischer, M. Rosay, M. A. Shapiro, J. R. Sirigiri, R. J. Temkin and P. P. Woskov, *Ieee T Plasma Sci*, 2006, **34**, 518-523.
39. M. K. Hornstein, V. S. Bajaj, R. G. Griffin and R. J. Temkin, *Ieee T Plasma Sci*, 2006, **34**, 524-533.
40. A. C. Torrezan, S. T. Han, M. A. Shapiro, J. R. Sirigiri and R. J. Temkin, 33rd International Conference on Infrared, Millimeter and Terahertz Waves, Pasadena, CA, 2008.

41. T. Idehara, T. Saito, I. Ogawa, S. Mitsudo, Y. Tatematsu, L. Agusu, H. Mori and S. Kobayashi, *Applied Magnetic Resonance* 2008, **34**, 265.
42. V. E. Zapevalov, V. V. Dubrov, A. S. Fix, E. A. Kopelovich, A. N. Kuftin, O. V. Malygin, V. N. Manuilov, M. A. Moiseev, A. S. Sedov, N. P. Venediktov and N. A. Zavolsky, Intl. Conf. Infrared, Millimeter, and Terahertz Waves, Busan, Korea, 2009.
43. K.-N. Hu, V. S. Bajaj, M. M. Rosay and R. G. Griffin, *J. Chem. Phys.*, 2007, **126**, 044512.
44. R. J. Barker, J. H. Booske, N. C. Luhmann and G. S. Nusinovich, *Modern Microwave and Millimeter-Wave Power Electronics*, Wiley IEEE Press, 2005.
45. G. S. Nusinovich, *Introduction to the Physics of Gyrotrons*, Johns Hopkins University Press, Baltimore, MD, 2004.
46. R. A. Cairns and A. D. R. Phelps, *Generation and Application of High Power Microwaves*, Taylor & Francis, London, UK, 1997.
47. C. J. Edgcombe, *Gyrotron Oscillators: Their Principles and Practice*, CRC Press, 1993.
48. A. P. Gaponov-Grekhov and V. L. Granastein, *Applications of High-Power Microwaves*, Artech House, 1994.
49. M. V. Kartikeyan, E. Borie and M. K. A. Thumm, *Gyrotrons: High Power Microwave Sources and Technologies*, Springer, New York, NY, 2004.
50. K. L. Felch, B. G. Danly, H. R. Jory, K. E. Kreischer, W. Lawson, B. Levush and R. J. Temkin, *Proceedings of the IEEE*, 1999, **87**, 752-781.
51. M. Botton, J. T.M. Antonsen, B. Levush, K. T. Nguyen and A. N. Vlasov, *IEEE Trans. Plasma Sci.*, 1998, **26**, 882-892.
52. S. N. Vlasov, L. I. Zagryadskaya and M. I. Petelin, *Radio Eng. Electron. Phys.*, 1975, **20**, 14-17.
53. J. L. Doane, in *Infrared and Millimeter Waves*, ed. K. J. Button, Academic Press, Inc., Editon edn., 1985, vol. 13, pp. 123-170.
54. P. W. Woskov, V. S. Bajaj, M. K. Hornstein, R. J. Temkin and R. G. Griffin, *IEEE Transactions on Microwave Theory and Techniques*, 2005, **53**, 1863-1869.
55. P. J. Allen, F. Creuzet, H. J. M. Degroot and R. G. Griffin, *J Magn Reson*, 1991, **92**, 614-617.
56. A. E. Bennett, C. M. Rienstra, M. Auger, K. V. Lakshmi and R. G. Griffin, *J. Chem. Phys.*, 1995, **103**, 6951-6958.
57. B. M. Fung, A. K. Khitrin and K. Ermolaev, *Jour. Magnetic Resonance*, 2000, **142**, 97-101.
58. K. R. Thurber and R. Tycko, *Jour Magn Resonance*, 2009, **196**, 84-87.
59. A. B. Barnes, M. L. Mak-Jurkauskas, Y. Matsuki, V. S. Bajaj, P. C. A. v. d. Wel, R. DeRocher, J. Bryant, J. R. Sirigiri, R. J. Temkin, J. Lugtenburg, J. Herzfeld and R. G. Griffin, *Jour. Magnetic Resonance*, 2009, **198**, 261–270.
60. A. B. Barnes, B. Corzilius, M. L. Mak-Jurkauskas, L. B. Andreas, V. S. Bajaj, Y. Matsuki, M. L. Belenky, J. R. Sirigiri, R. J. Temkin, J. Herzfeld and R. G. Griffin, *PhysChemChemPhys*, 2010, **XX**, XXXX-XXXX.
61. A. Hackmann, H. Seidel, R. D. Kendrick, P. C. Myhre and C. S. Yannoni, *J Magn Reson*, 1988, **79**, 148-153.
62. K. R. Thurber and R. Tycko, *Jour Magn Resonance*, 2009, **195**, 179-196.
63. M. M. Rosay, Ph.D. Thesis, Massachusetts Institute of Technology, 2001.
64. K. N. Hu, Ph.D. Thesis, MIT, 2008.
65. G. T. Debelouchina, M. J. Bayro, P. C. A. v. d. Wel, M. A. Caporini, A. B. Barnes, M. Rosay, W. Maas and R. G. Griffin, *PhysChemChemPhys*, 2010, **XX**, XXXX-XXXX.